Article

Facile and Green Fabrication of Microwave-Assisted Reduced Graphene Oxide/Titanium Dioxide Nanocomposites as Photocatalysts for Rhodamine 6G Degradation

Andri Hardiansyah, William J. Budiman, Nurfina Yudasari, Isnaeni, Tetsuya Kida, and Arie Wibowo*

Read Online

| ACCESS | Metrics & More | Article Recommendations |

ABSTRACT: Organic pollutants, such as synthetic dyes, are treated to prevent them from contaminating natural water sources. One of the treatment methods is advanced oxidation process using a photocatalyst material as the active agent. However, many photocatalysts are hindered by their production cost and efficiency. In this study, nanocomposites consisting of reduced graphene oxide and titanium dioxide (rGO/TiO_2) were prepared by a simple and green approach using the microwave-assisted method, and we utilized a graphene oxide (GO) precursor that was fabricated through the Tour method. The ratios of rGO/TiO_2 in nanocomposites were varied (2:1, 1:1, and 1:2) to know the influence of rGO on the photocatalytic performance of the nanocomposites for rhodamine 6G degradation. Transmission electron microscopy (TEM) observation revealed that a transparent particle with a sheetlike morphology was detected in the rGO sample, suggesting that a very thin film of a few layers of GO or rGO was successfully formed. Based on scanning electron microscopy (SEM) observation, the rGO/TiO_2 nanocomposites had a wrinkled and layered rGO structure decorated by TiO_2 nanoparticles with average diameters of 125.9 ± 40.6 nm, implying that rGO layers are able to prevent TiO_2 from agglomeration. The synthesized product contained only rGO and TiO_2 in the anatase form without impurities that were proven by Raman spectra and X-ray diffraction (XRD). The nanocomposite with rGO/TiO_2 ratio 1:2 (composite C) was found to be the best composition in this study, and it was able to degrade $82.9 \pm 2.4\%$ of the rhodamine 6G after UV irradiation for 4 h. Based on a time-resolved photoluminescence study at wavelength emission 500 nm, the average decay lifetime of R6G-rGO/TiO_2 composites (2.91 ns) was found to be longer than that of the R6G-TiO_2 sample (2.05 ns), implying that the presence of rGO in rGO/TiO_2 composites successfully suppressed the electron−hole recombination process in TiO_2 and significantly improved their photocatalytic performance. This study showed that the rGO/TiO_2 nanocomposites synthesized through relatively simple and eco-friendly processes display promising prospects for photocatalytic degradation of dyes and other recalcitrant pollutants in a water stream.
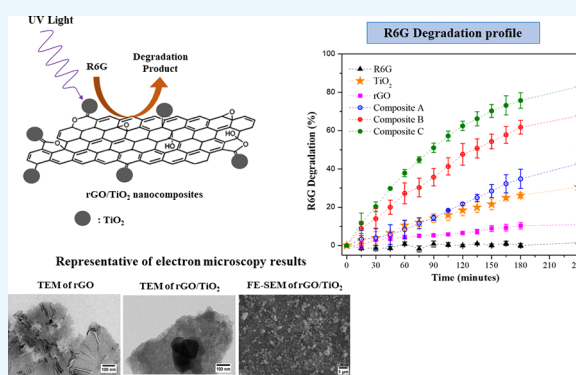
1. INTRODUCTION

In the past decades, industrial effluents that were released into the aquatic environment without proper treatment have contributed greatly toward water pollution. In textile industries alone, 1.5 million liters of effluents per day are released into natural water sources from a fabric mill producing 60×10^4 m of textile fabrics.[1] Synthetic dyes, which are abundant in effluents, are used extensively in textile industries because of their higher color yield, lower water usage and steam consumption, shorter cycle time, and cheaper cost compared to natural dyes.[1,2] On the other hand, most synthetic dyes are categorized into recalcitrant pollutants, which are difficult to degrade completely through conventional physical, chemical, and biological processes.[1,3,4] Many serious problems such as color pollution, reduced water photosynthetic activity, physiological disorder, and cancer in the human body can

occur if these synthetic dyes are released directly to the environment untreated.[1] Thus, an alternative method is needed to overcome these problems.

Advanced oxidation process (AOP) technology such as Fenton-based catalysts[3,5,6] and photocatalysts[3,7] can eliminate persistent organic pollutants through total mineralization into CO_2 and H_2O, which are harmless to the environment.[4] Photocatalytic degradation is an attractive solution for synthetic dye removal in a water stream because of the

abundance of its energy source in sunlight and no other chemical substances being needed, making it cheaper compared to other methods.[8−10] To date, there are various nanostructure materials that have been explored as photocatalysts such as graphitic carbon nitride-based composites,[11−13] transition-metal selenides and diselenides,[14] $PrVO_4$,[15] Tl_4CdI_6,[16] and $Nd_2Sn_2O_7$.[17] Among them, titanium oxide (TiO_2) is one of the semiconductors that is commonly used as an active material in the photocatalytic degradation process because TiO_2 is relatively cheaper, commercially available, photochemically stable, and nontoxic.[18,19] However, TiO_2 has several weaknesses such as a fast recombination phenomenon, low specific surface area, particle agglomeration, and high band gap, which may reduce its performance and hinder it from visible-light photoexcitation.[20,21] Thus, many researchers devoted their efforts to enhancing their performance of the TiO_2-based photocatalytic degradation process.[22]

To solve this problem, TiO_2 can be paired up with reduced graphene oxide (rGO) to become rGO/TiO_2 nanocomposites. The presence of rGO in rGO/TiO_2 nanocomposites could significantly improve the photocatalytic performance of TiO_2 because rGO has a high surface area that prevents agglomeration of TiO_2 particles, allowing electron transfer from TiO_2 to rGO to suppress the electron−hole recombination process.[23,24] This binary nanocomposite could be prepared by covalent attachment,[25] alkaline hydrothermal synthesis,[26] microwave-assisted synthesis,[27] and sol−gel synthesis preceded by GO spray-drying.[26−28]

It is to be noted that most of the mentioned studies used graphene oxide (GO) synthesized through the Hummers method with little modification. However, this method might be harmful to the environment because it may produce toxic NO and NO_2 gases from the decomposition of HNO_3.[29] In this context, utilization of the Tour method is more eco-friendly than the Hummers method to produce the GO precursor because the Tour method employs H_3PO_4 instead of HNO_3, avoiding toxic gas production, to obtain a high yield of oxidized GO as its product.[30] Thus, in this study, rGO/TiO_2 nanocomposites were prepared by a green and simple method, where the GO precursor was synthesized by the Tour method and GO reduction was performed by microwave irradiation. Microwave irradiation was used to reduce GO because (i) this method is relatively safe and harmless compared to chemical reduction that used toxic chemicals, such as hydrazine, as the reducing agent;[31] (ii) this method is able to produce uniform and rapid heat throughout the samples while consuming less energy and time;[32] (iii) Iskandar et al. found that rGO that was produced by the microwave-assisted method achieve higher electrical conductivity (1180 S m$^{−1}$) than the rGO synthesized by the Hummers (5 S m$^{−1}$) and Tour (10 S m$^{−1}$) methods.[31] To the best of our knowledge, this combination method (Tour method for GO production and microwave irradiation for GO reduction) to prepare rGO/TiO_2 nanocomposites has not been explored yet. The structure and morphology of the synthesized rGO/TiO_2 nanocomposites were evaluated through microscopy and spectroscopy. The effect of rGO on the nanocomposite's photocatalytic performance through the photocatalyst was investigated by varying the rGO/TiO_2 ratio in nanocomposites.

2. RESULTS AND DISCUSSION

2.1. GO Formation through the Tour Method.
To confirm that GO was successfully prepared from the graphite precursor through the Tour method, both the graphite precursor and the synthesized product were characterized using XRD and the Raman spectroscopy method. As can be seen in Figure 1a, XRD patterns of the graphite precursor and
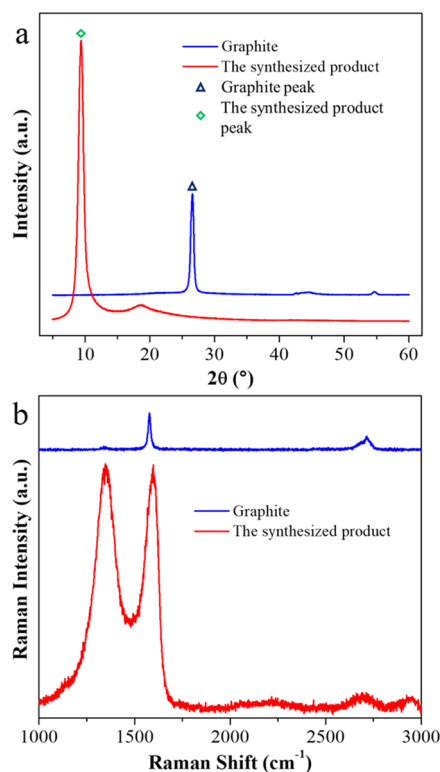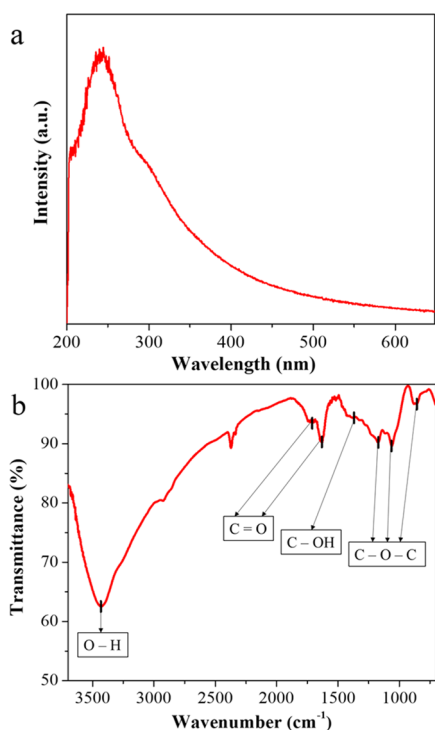

Figure 1. Characterization results of the graphite precursor (blue) and the synthesized product (red) using (a) XRD and (b) Raman spectroscopy.

the synthesized product showed main peaks at 2θ value of 26.5 and 9.4°, respectively, which are correlated with the interlayer spacing distances of graphite (3.4 Å) and GO (9.4 Å).[33] The increased interlayer spacing distance value in the synthesized product can be attributed to the presence of hydroxyl, carboxyl, or epoxy functional groups that commonly occurred in GO. Since the peak that was associated with GO (9.4°) was observed and the peak that was associated with graphite (26.5°) disappeared in the synthesized product, it might be considered that GO was successfully prepared in the synthesized product. Further characterization using Raman spectroscopy was implemented to confirm this hypothesis.

Raman spectroscopy results of the graphite precursor and the synthesized product are presented in Figure 1b. Raman spectroscopy of the graphite precursor showed two characteristic peaks at 1578 and 2715 cm$^{−1}$, which correspond to the G band and the 2D band, respectively. The G band represents in-plane carbon sp^2 stretching,[34] while the 2D or G′ band represents the number of graphene layers in graphitic materials and is caused by second-order phonon processes.[35,36] Raman spectroscopy of the synthesized product displayed the absence of the 2D band's peak and the presence of the G band's peak (1601 cm$^{−1}$) with intensity higher than the G band of the graphite precursor. Significant increment of the G band in the synthesized product suggested that the exfoliation process of graphite occurred because the G band's peak is narrow and intense in single-layered graphene and becomes broad and

weak with the addition of new layers in graphite. Interestingly, a new peak was observed in the synthesized product at 1325 cm^{-1}, which is correlated with the D band and represents the structural disorder of GO. The appearance of two characteristic peaks of GO (G and D bands) and the absence of a characteristic peak of graphitic materials (2D band) suggested that GO might be formed in the synthesized product. It is to be noted that the higher ratio between the D band and G band (I_D/I_G value) suggests the higher quality of the GO because it may indicate a higher degree of oxidation, which may cause the disordered structure in GO.[30] Considering that the I_D/I_G value of the synthesized GO in this study (2.33) is higher than the I_D/I_G value of GO that was synthesized by the Hummers method (0.95−1.60),[27,35] it can be concluded that the GO that was obtained from the Tour method has a better quality than that obtained by the Hummers method.

Additional characterizations using UV−vis and FTIR spectroscopies were carried out on the synthesized product sample for further confirmation (Figure 2). UV−vis spectros-


Figure 2. Characterization results of the synthesized product using (a) UV−vis and (b) FTIR spectroscopies.

copy results of the synthesized product (Figure 2a) showed a main peak at 230 nm with a shoulder at 300 nm, which belongs to electronic transitions in GO.[37] The 230 nm peak was correlated with the $\pi \rightarrow \pi^*$ electronic transition from C=C bonding, while the 300 nm peak was correlated with the n $\rightarrow$ π^* electronic transition from the free electron pair of the carbonyl group.

The FTIR result of the synthesized product (Figure 2b) showed various peaks, which were assigned to various bonding vibrations.[38−40] The broad peak at 3433 cm^{-1} was assigned to the O−H vibration in the hydroxyl group. Peaks at 1710 and 1632 cm^{-1} were attributed to the C=O vibration in the carbonyl or carboxyl group. The peak at 1369 cm^{-1} was attributed to the C−OH vibration in the carboxyl group. Peaks at 1171, 1064, and 856 cm^{-1} were attributed to the C−O−C

vibration in the epoxide group. It can be said that GO was detected in the synthesized product due to the existence of peaks that correlated with oxygen-containing functional groups such as hydroxyl, carbonyl, carboxyl, or epoxide. Based on sample evaluation using XRD, Raman, UV−vis, and FTIR methods, it can be concluded that GO was successfully prepared from the graphite precursor through the Tour method.

2.2. Fabrication of rGO/TiO$_2$ Composites. After achieving the GO precursor through the Tour method, GO was mixed with TiO$_2$ with various compositions followed by microwave-assisted reduction to obtain rGO/TiO$_2$ nanocomposites, and their morphologies were evaluated by TEM and SEM methods, while their elemental distributions were determined by the EDS method. The TEM observation revealed that a transparent particle with a sheetlike morphology was detected in the rGO sample (Figure 3a),
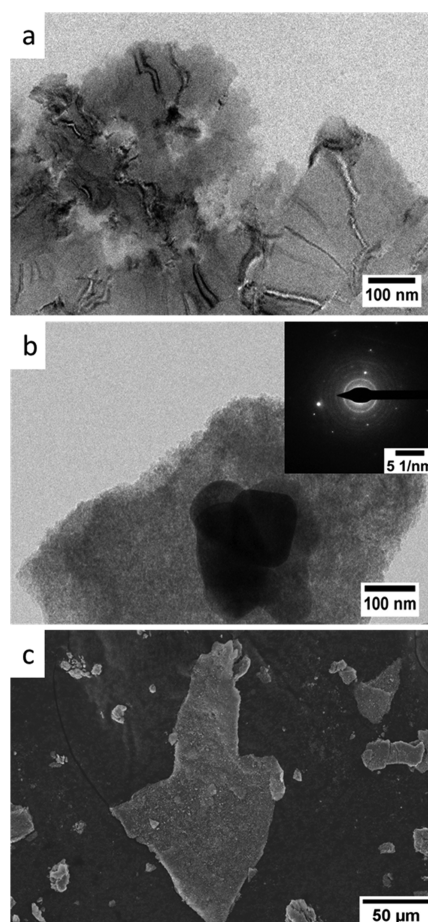

Figure 3. TEM observation of (a) rGO and (b) composite C. (c) Low-magnification SEM observation of composite C as a representative of a nanocomposite sample.

which is consistent with the TEM image of rGO observed by Stobinski et al.[41] The high transparency of sheet particles in the rGO sample suggested that a very thin film of a few layers of GO or rGO was successfully formed as a result of the exfoliation process that occurred during GO formation through the Tour method and followed by a reduction step.

Meanwhile, TEM observation of composite C as a representative of a nanocomposite sample unveiled the presence of a transparent sheet particle and irregular particles
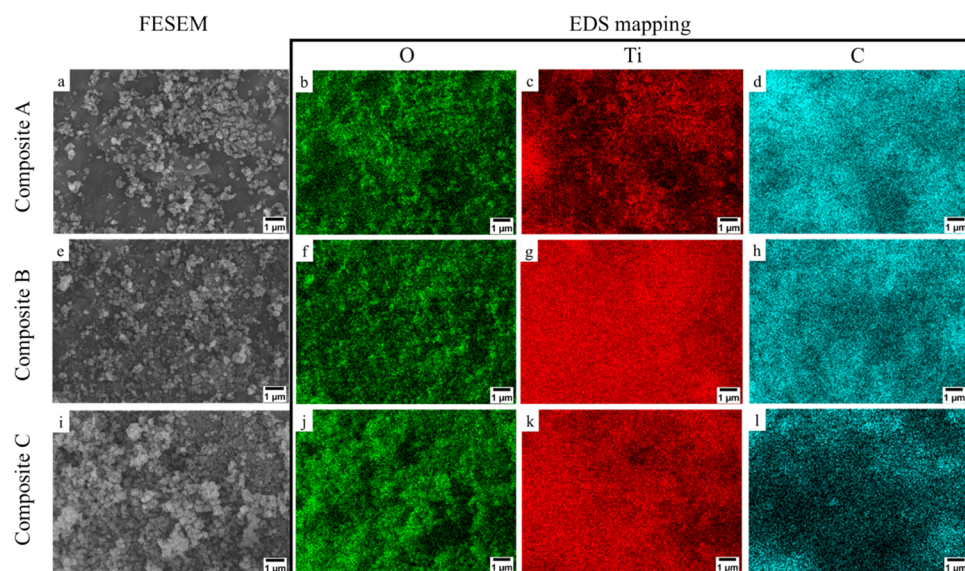
Figure 4. FE-SEM images of (a) composite A and its EDS mapping results for (b) O, (c) Ti, and (d) C elements. FE-SEM images of (e) composite B and its EDS mapping results for (f) O, (g) Ti, and (h) C elements. FE-SEM images of (i) composite C and its EDS mapping results for (j) O, (k) Ti, and (l) C elements.

with a particle size of 127.4 nm (Figure 3b). Transparency of sheet particles in the composite sample is lower than that in the rGO sample, implying that rGO particles might be covered by other particles. Further characterization using the selected area electron diffraction (SAED; inset of Figure 3b) method confirmed the presence of TiO_2 in the composite sample with Miller indices of (101), (004), (200), (211), and (204) (JCPDS No. 21-1272). Based on the TEM and SAED results, the irregular particles and sheet particles may be identified as TiO_2 and rGO, respectively.[42] Low-magnification SEM observations on composite C as a representative of nanocomposite samples revealed that micron-sized particles (125.9 ± 40.6 μm) with a sheet structure were observed (Figure 3c). These sheet particles might be associated with rGO in the nanocomposites sample.[43]

SEM observation at a higher magnification unveiled that nanoparticles were observed on the surface of sheet particles in all rGO/TiO_2 nanocomposites with average sizes of 125.9 ± 40.6, 127.3 ± 27.2, and 128.6 ± 40.5 nm for composites A (Figure 4a), B (Figure 4e), and C (Figure 4i), respectively. EDS mapping of O (Figure 4b,f,j) and Ti (Figure 4c,g,k) elements of nanocomposites is correlated with nanoparticles, and their intensity increased as the TiO_2 content in nanocomposites increased, while EDS mapping of the C element (Figure 4d,h,l) showed a reduced intensity as the TiO_2 content in the composites increases. Summary of the elemental composition of rGO/TiO_2 samples from EDS results is presented in Table 1. According to SEM and EDS results, it can be concluded that TiO_2 nanoparticles were formed on the surface of rGO with the sheet structure.

Raman spectra of pristine TiO_2, rGO, and their nanocomposites are presented in Figure 5. Raman spectra of the pristine TiO_2 sample showed peaks at 136, 196, 395, 514, and 638 cm^{-1}, which belong to TiO_2 in the anatase form.[44] While Raman spectra of the pristine rGO sample showed a pair of weak peaks at 1344 and 1598 cm^{-1} (inset of Figure 5), which are associated with the D band and G band of rGO, respectively.[26] Raman spectra of rGO/TiO_2 nanocomposite samples demonstrated the presence of anatase and rGO peaks

Table 1. EDS Elemental Composition of rGO/TiO_2 Samples

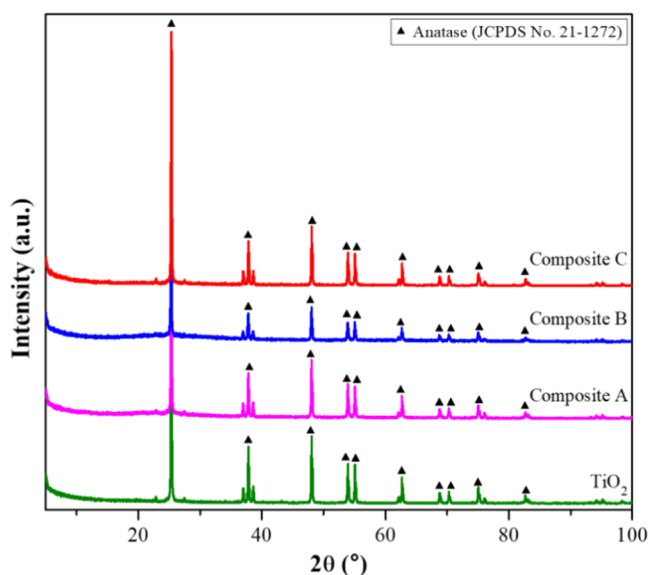| sample	wt %		
	O	Ti	C
rGO/TiO_2 (2:1)	29.6 ± 1.9	26.5 ± 1.2	43.9 ± 1.8
rGO/TiO_2 (1:1)	32.4 ± 1.3	30.8 ± 1.0	36.8 ± 0.4
rGO/TiO_2 (1:2)	45.6 ± 2.2	41.9 ± 1.6	12.5 ± 2.3
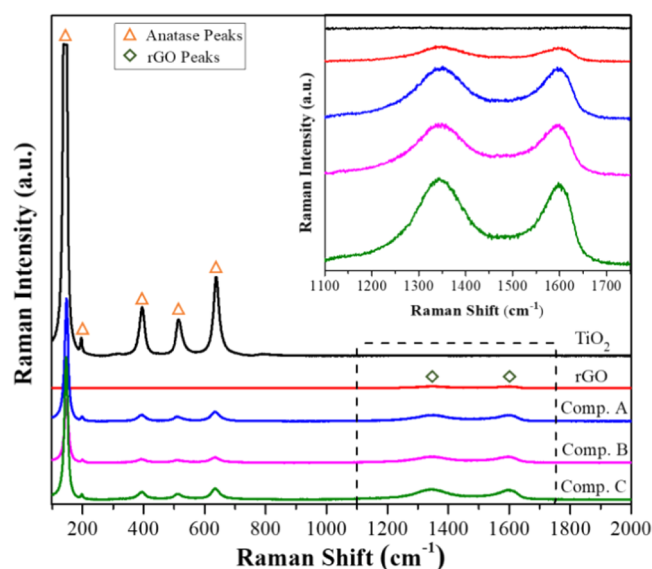
Figure 5. Raman spectra of pristine TiO_2, rGO, and rGO/TiO_2 nanocomposite samples with an inserted magnification at the rGO peak region. Certain peaks of TiO_2 and rGO are marked with markers.

in all nanocomposite samples, suggesting that TiO_2 has successfully been integrated into rGO layers and no other substances were formed. Anatase peaks of rGO/TiO_2 nanocomposite samples had a lower intensity than the pristine TiO_2 sample because TiO_2 fractions in nanocomposite samples are

lower than those of the pristine TiO$_2$ sample. On the other hand, rGO peaks in the nanocomposite samples had a higher intensity than the pristine rGO sample because the integrated TiO$_2$ nanoparticles may act as disordered and defect structures while also stretching the sp^2 bond of rGO.[26] These phenomena lead to the higher D band and G band intensities. The I_D/I_G values of D and G bands of GO, rGO, rGO/TiO$_2$ (2:1), rGO/TiO$_2$ (1:1), and rGO/TiO$_2$ (1:2) were calculated to be 2.33, 2.21, 1.94, 2.39, and 2.42, respectively. The higher I_D/I_G value of GO compared to rGO was correlated with the degree of structural disorder caused by an abundance of oxide groups in GO. An increase in the I_D/I_G value in rGO/TiO$_2$ samples with increasing TiO$_2$ content could be assigned to the increased structural disorder in the graphitic structure because of TiO$_2$ particle's presence in the rGO layers.[26]

The XRD spectra of TiO$_2$ and the composites (Figure 6) showed diffraction peaks that are correlated with the anatase

Figure 6. XRD spectra of pristine TiO$_2$ and rGO/TiO$_2$ nanocomposite samples. Certain peaks of anatase TiO$_2$ according to the JCPDS No 21-1272 database are marked with markers.

peaks from JCPDS No. 21-1272. These XRD results are consistent with the Raman results, indicating the presence of anatase in TiO$_2$ and the composite sample. rGO peaks could not be observed in XRD results of composite samples due to their broad peak and amorphous nature.[41] The crystallite size of TiO$_2$ and the nanocomposite samples can be calculated from their XRD results using the Scherrer formula as follows.[45]

$$D = \frac{K\lambda}{\beta \cos\theta} \tag{1}$$

where D is the crystallite size, K is the shape factor, λ is the X-ray wavelength, β is the line broadening at full width at half-maximum (FWHM), and θ is the Bragg angle.

According to the Scherrer formula, the crystallite sizes of TiO$_2$, composite A, composite B, and composite C are 131.7, 75.5, 77.1, and 83.9 nm, respectively. The rGO/TiO$_2$ composites with a higher rGO content have smaller anatase crystallite sizes that were also reported by other studies.[46,47] The presence of rGO inhibited the TiO$_2$ crystallite growth due to many possible nucleation sites on rGO.[48,49]

The dissolution−crystallization process of TiO$_2$ can be controlled by tuning the pH of the solution. TiO$_2$ powder can be dissolved in an acidic condition of a Tour solution to form TiO^{2+} ions. Dissolved TiO^{2+} species may attach to C=O, COOH, and C−OH bonds of GO oxide groups as the anchor of further growth. Adding NaOH to the solution will provide an alkaline condition that will lead to crystallization of Na$^+$, OH$^-$, and TiO^{2+} ions into the titanate complex such as Na$_2$Ti$_3$O$_7$.[50,51] Titanate crystals nucleated at these GO sites, especially the C=O site.[49] The heating process of microwave irradiation reduced GO layers into rGO through the removal of oxide groups.[52] Then, H$^+$ ions can substitute the Na site on Na$_2$Ti$_3$O$_7$ during the washing process using HCl and finally the titanate complex would transform into TiO$_2$ during the drying process through the reaction described in eq 2.[22] Based on these results, the formation mechanism of rGO/TiO$_2$ nanocomposites in this study is illustrated in Figure 7.

$$Na_2Ti_3O_7 \rightarrow H_2Ti_3O_7 \rightarrow H_2Ti_6O_{13} \rightarrow TiO_2 \tag{2}$$
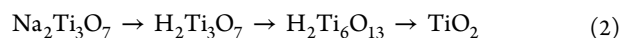
2.3. Photocatalytic Degradation of Rhodamine 6G (R6G). The R6G degradation profile of each sample under UV irradiation is shown in Figure 8. Prior to studying the
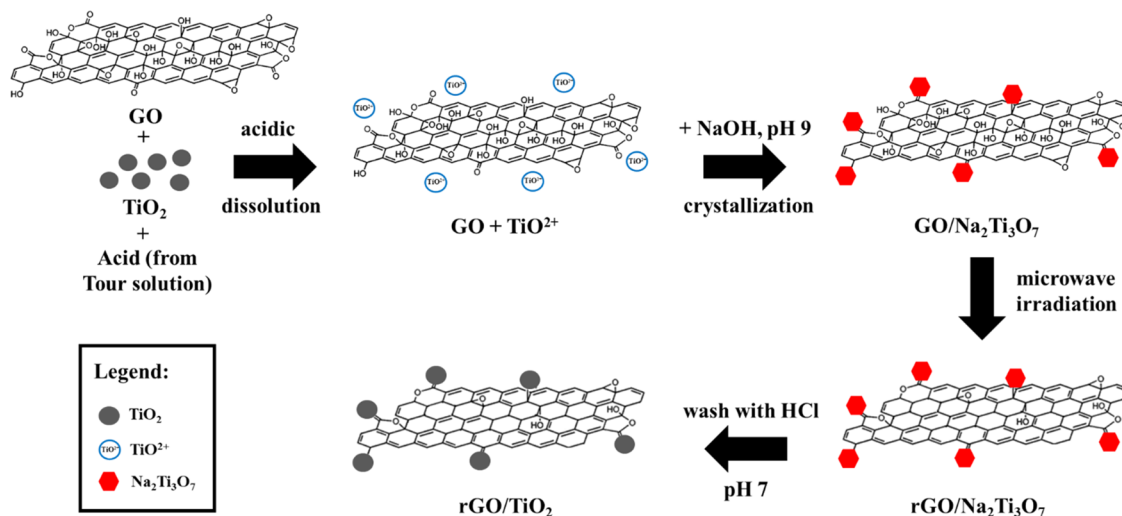

Figure 7. Schematic illustration of the formation mechanism of rGO/TiO$_2$ nanocomposites.
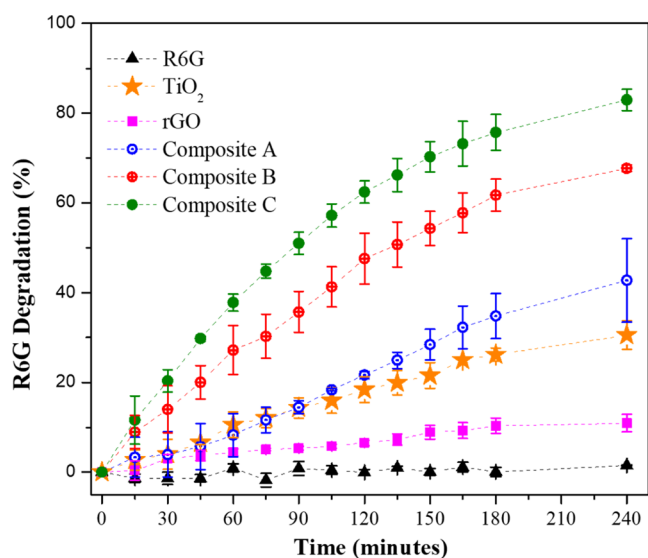
Figure 8. Degradation of R6G measured through UV−vis spectroscopy in the photocatalysis experiment.

photocatalytic performance of composites, the R6G degradation profiles of the pristine R6G solution, rGO, and TiO$_2$ were examined to know the effect of each component on the photocatalytic performance of composites under UV irradiation. As can be seen in Figure 8, the R6G concentration of the pristine R6G solution remains the same as their original concentration after UV irradiation for 4 h, suggesting that photodegradation did not occur on the pristine R6G solution.

The effect of each component of rGO/TiO$_2$ composites on the R6G degradation profile was explored by mixing the R6G solution with rGO and TiO$_2$ separately and exposing to UV irradiation for 4 h. In the presence of rGO in the R6G solution, the R6G concentration in a solution decreases to about 10.9 ± 1.9% after UV irradiation for 4 h. It is to be noted that rGO has a residual oxide function group and vacancies as leftovers from the GO reduction process may facilitate R6G adsorption through $\pi-\pi$ and/or electrostatic interaction, leading to the slight decrease of the R6G concentration in solution.[53] Considering that the curve was stagnant at around 10.9%, it could be implied that rGO's adsorption capacity in this study was reached, which prevented further R6G adsorption. The reduction of the R6G concentration is lower compared to that of a previous study that introduced continuous stirring during the adsorption process.[54] Meanwhile, the R6G concentration in solution was reduced by about 30.6 ± 3.2% if the R6G solution containing TiO$_2$ was irradiated with UV for 4 h. It is noteworthy that Pu et al. reported that the R6G adsorption behavior of pure TiO$_2$ was ∼5% with a TiO$_2$:R6G ratio (w/w) of 50:1.[54] Since the TiO$_2$:R6G ratio (w/w) that was used in this study (1:1) is significantly lower than the work of Pu et al. (50:1), it could be expected that the role of adsorption on reduction of the R6G concentration is insignificant in this study. Thus, the R6G degradation profile of the TiO$_2$ sample could be associated with photocatalytic degradation of R6G in the presence of TiO$_2$ as a photocatalyst. It should be noted that most studies used a higher concentration of the catalyst compared to its pollutant model, which explained its relatively low degradation by 4 h of photocatalysis.[26,55,56]
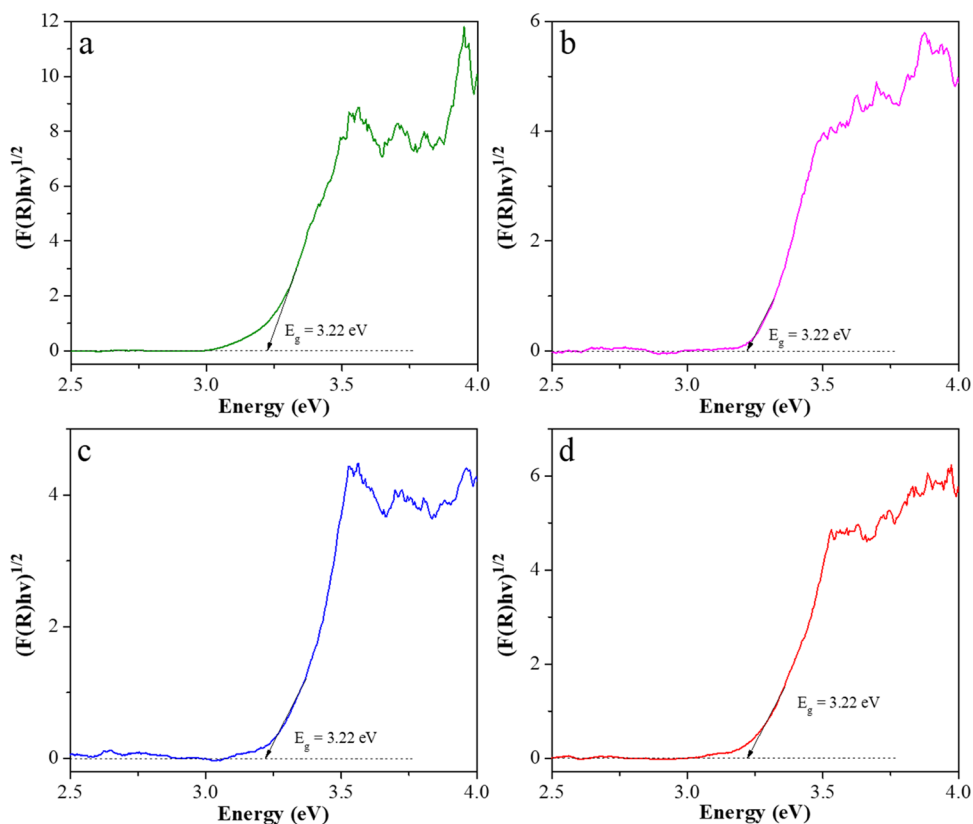
Figure 9. Tauc plot and band-gap value of (a) TiO$_2$, (b) composite A, (c) composite B, and (d) composite C derived from their DR UV−vis spectra.

A greater decrease of the R6G concentration in solution could be obtained by mixing the R6G solution with the rGO/TiO$_2$ composites. As can be seen in Figure 8, the R6G concentration in the rGO/TiO$_2$ composite samples decreases by around 42.7−82.9% after UV irradiation for 4 h. These results indicate that combining rGO and TiO$_2$ as composites led to a substantial improvement on R6G degradation, which is significantly higher than the sole adsorption effect of pristine rGO (10.9 ± 1.9%) and the sole photocatalytic degradation effect of pristine TiO$_2$ (30.6 ± 3.2%). This phenomenon might have occurred due to the presence of rGO in the rGO/TiO$_2$ composites, which could have acted as dye adsorption sites and electron acceptors that were generated during photoexcitation. By moving the electron from TiO$_2$ to rGO, which has excellent electron-transfer performance,[26] the recombination process could be prevented,[28] thus improving the photocatalytic activity of the photocatalyst.[57,58]

As can be seen in Figure 8, composite C has a higher R6G degradation (82.9 ± 2.4%) than composite A (42.7 ± 9.3%) and composite B (67.7 ± 0.7%). It is well known that tuning the ratio of rGO and TiO$_2$ in the rGO/TiO$_2$ composites may affect the composite's photoactivity. In this case, a higher rGO content in the system may disturb the absorption of the photon by TiO$_2$ due to scattering and absorption by carbon in rGO.[57] On the other hand, the low rGO content can be insufficient to facilitate electron transfer from photogeneration in TiO$_2$ to prevent electron−hole recombination.[28] In this case, composite C, which had the lowest rGO composition, was the optimal composition as indicated by its high R6G degradation.

To understand this phenomenon, further characterizations are needed to reveal the role of rGO on the catalytic performance of rGO/TiO$_2$ composites. In this study, the diffuse reflectance UV−vis (DR UV−vis) spectroscopy method was performed on TiO$_2$ and rGO/TiO$_2$ nanocomposite samples to understand the influence of rGO on the TiO$_2$ band-gap value in rGO/TiO$_2$ composites. The resulting reflectance was processed into band-gap energy using the Tauc plot curve through the Kubelka−Munk equation as follows.[59]

$$f(R) = \frac{(1 - R)^2}{2R} = \frac{\alpha}{s} \quad (3)$$

where R is the reflectance ($R = R$ sample/R reference), α is the absorption coefficient, and s is the scattering coefficient. This is the equation of a straight line whose interception with the abscissa axis corresponds to a band-gap energy.

The Tauc plot of TiO$_2$ and rGO/TiO$_2$ nanocomposites and their band-gap energy determination are presented in Figure 9. As can be seen in Figure 9a, the TiO$_2$ band-gap value was 3.22 eV, which is similar to the TiO$_2$ band gap in the anatase form (3.2 eV).[60] This result is consistent with Raman and XRD results, indicating the presence of anatase in the TiO$_2$ sample. Interestingly, the band-gap value of all composite samples (Figure 9b−d) was similar to the TiO$_2$ band-gap value (3.22 eV), suggesting that the presence of rGO in the composite did not affect the TiO$_2$ band-gap value.[61] These results imply that band-gap modification might not be the reason for the increment phenomena of the catalytic performance of rGO/TiO$_2$ composites.

Further study using the photoluminescence spectroscopy method was conducted on R6G, R6G with rGO, R6G with TiO$_2$, and R6G with composite C samples as the representative

of the rGO/TiO$_2$ composite sample. The photoluminescence spectra results of all samples are shown in Figure 10a. After UV
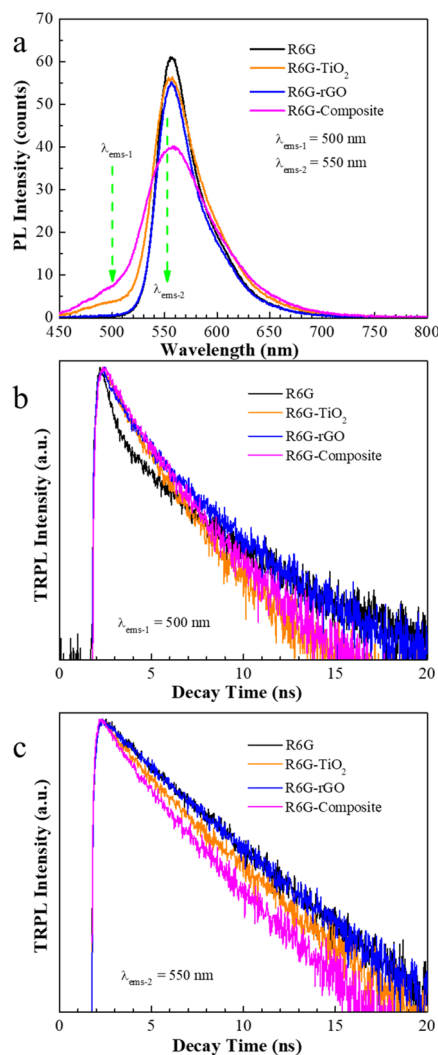
Figure 10. (a) Photoluminescence of R6G samples with and without a catalyst after UV irradiation; time-resolved photoluminescence of R6G samples with and without a catalyst after UV irradiation at (b) λ_{ems} = 500 nm and (c) λ_{ems} = 550 nm.

irradiation, R6G-rGO, R6G-TiO$_2$, and R6G-composite samples showed a lower luminescent intensity than the pristine R6G sample, with the greatest reduction of luminescent intensity being observed on the R6G-composite sample. Even though the laser that was used in this RT-PL study (420 nm = 2.95 eV) has a lower energy than the anatase band gap (3.2 eV[60]), a small and broad peak at around 500 nm was only observed on the TiO$_2$-containing samples (R6G-TiO$_2$ and R6G-rGO/TiO$_2$), suggesting that this peak might correlate with TiO$_2$. Mathew et al. found that TiO2 nanoparticles that were prepared by the hydrothermal method showed emission peaks at 387, 421, 485, 530, and 574 nm.[60] These peaks are correlated with the presence of defect levels on TiO$_2$ that were caused by the oxygen vacancies. Thus, the presence of a broad peak at around 500 nm on TiO$_2$-containing samples might indicate the presence of the defect level of TiO$_2$ nanoparticles in our sample.

Charge separation and energy transfer on our samples were studied by conducting time-resolved photoluminescence

Table 2. Fitting Results of Time-Resolved Photoluminescence and Energy-Transfer Efficiency

sample	τ_{ave} (ns) at λ = 500 nm	τ_{ave} (ns) at λ = 550 nm	k_{ET} (10^8 s^{-1}) at λ = 550 nm	n_{ET} (%) at λ = 550 nm
R6G	1.35	3.99		
R6G + TiO$_2$	2.05	3.15	6.68	21.05
R6G + rGO	2.25	3.89	0.64	2.51
R6G + composite	2.91	2.46	15.58	38.35

(TRPL) at two wavelength emissions, i.e., 500 nm (luminescence of TiO$_2$ nanoparticles) and 550 nm (luminescence of dye R6G). The TRPL signals for 500 and 550 nm are shown in Figure 10b and c, respectively. The average decay lifetime (τ_{ave}), energy-transfer rate (k_{ET}), and energy-transfer efficiency (n_{ET}) were calculated from the TRPL signal using eqs 4−6 as follows[62,63]

$$\tau_{ave} = \sum_{i=1}^{2} \frac{a_i \tau_i^2}{a_i \tau_i} \tag{4}$$

$$k_{ET} = \frac{1}{\tau_{ave}(R6G + catalyst)} - \frac{1}{\tau_{ave}(R6G)} \tag{5}$$

$$n_{ET} = 1 - \frac{\tau_{ave}(R6G + catalyst)}{\tau_{ave}(R6G)} \tag{6}$$

The calculation results are presented in Table 2. For TRPL at 500 nm (2.48 eV), the decay lifetime of the R6G sample was found to be shorter than the others, implying the negative values of k_{ET} and n_{ET} for the R6G sample at this wavelength (data is not shown). Thus, it can be concluded that there is no energy transfer from R6G to TiO$_2$ or rGO at 500 nm. Furthermore, the average decay lifetime of R6G-rGO/TiO$_2$ composites (2.91 ns) is longer than the R6G-TiO$_2$ sample (2.05 ns), implying that the presence of rGO in rGO/TiO$_2$ composites successfully suppressed the electron−hole recombination process in TiO$_2$. This phenomenon occurred because the photogenerated electron can be transferred from TiO$_2$ to rGO, and this phenomenon might be crucial for the significant increment of the photocatalytic performance.[23,24]

On the other hand, TRPL at 550 nm (2.25 eV) showed that energy transfer can occur at 550 nm, with R6G composites showing the highest energy-transfer efficiency (around 38.35%). This means that more electrons will be transferred to TiO$_2$ defect levels for generating radicals. Therefore, luminescent quenching will be strongly observed. The generation of radicals is one of the main reasons for luminescent quenching and degradation of the dye R6G.[64]

Based on these TRPL results, a simple diagram of energy transfer in our study is illustrated in Figure 11. There is an energy-transfer process that occurs between dye R6G and TiO$_2$ or rGO. Excited electrons from R6G were then transferred to

defect levels of TiO$_2$, as noted by ET in the diagram. These electrons can be used for the oxidation process to make O$_2$ radicals. Some electrons may return back to the valence band of R6G by giving out luminescence. Meanwhile, another radical was generated due to charges (from holes) in the R6G. We assume that holes and electrons will generate radicals. Each photocatalysis process that uses TiO$_2$ is strongly predicted to have O^{2-} and $^-$OH radicals, since charge carriers (electrons and holes) near the surface of TiO$_2$ will easily react with surrounding molecules or dyes and generate radicals.[65]

3. CONCLUSIONS

Based on characterization results, it can be concluded that the rGO/TiO$_2$ nanocomposites were successfully prepared by the microwave-assisted method with the GO precursor fabricated through the Tour method. The presence of rGO in the rGO/TiO$_2$ nanocomposites was able to enhance the photocatalytic performance of TiO$_2$ due to effective electron transfer from TiO$_2$ to rGO, which prevents fast recombination, good ability to promote formation of TiO$_2$ nanoparticles, and efficient dye adsorption into nanocomposites. Composite C with rGO:TiO$_2$ ratio 1:2 was found to be the best composition in this study with R6G degradation 82.9 ± 2.4% after UV irradiation for 4 h. Based on time-resolved photoluminescence study at wavelength emission 500 nm, the average decay lifetime of R6G-rGO/TiO$_2$ composites (2.91 ns) is longer than that of the R6G-TiO$_2$ sample (2.05 ns), implying that the presence of rGO in rGO/TiO$_2$ composites successfully suppressed the electron−hole recombination process in TiO$_2$ and significantly improved their photocatalytic performance. It is hoped that the simple and green synthesis of rGO/TiO$_2$ nanocomposites proposed in this study may encourage a new perspective of eco-friendly fabrication of rGO/TiO$_2$ nanocomposites and their utilization as a promising photocatalyst for photocatalytic degradation of dyes and other recalcitrant pollutants in a water stream.

4. EXPERIMENTAL SECTION

4.1. Materials. Graphite, potassium permanganate (KMnO$_4$), phosphoric acid (H$_3$PO$_4$), sulfuric acid (H$_2$SO$_4$), hydrogen peroxide (H$_2$O$_2$), hydrochloric acid (HCl), titanium (IV) oxide (TiO$_2$, in the anatase form), sodium hydroxide (NaOH), and rhodamine 6G (R6G) were purchased from Sigma-Aldrich. All chemicals were of proanalytical (p.a.) grade and used as received without further purification.

4.2. Synthesis of Reduced Graphene Oxide/Titanium Dioxide (rGO/TiO$_2$). Graphene oxide (GO) was synthesized by the Tour method.[30,66] Briefly, expanded graphite was oxidized with KMnO$_4$ in an acidic solution of H$_2$SO$_4$/H$_3$PO$_4$ (9:1), stopped with the addition of ice and H$_2$O$_2$, and washed with 5% HCl and deionized (DI) water three times each to yield graphene oxide as the product. Then, 6.6 mL of water-dispersed GO (3.8 mg/mL) was diluted with DI water into 50 mL of GO (0.5 mg/mL). Three different quantities of TiO$_2$ (anatase) powder were added into the GO dispersion to create
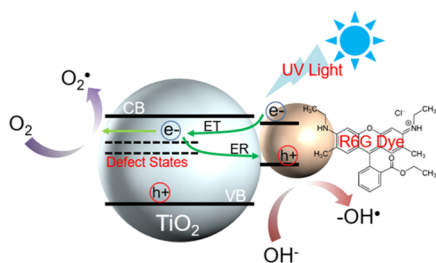

Figure 11. Proposed energy-transfer and charge separation diagram.

three different compositions of GO:TiO$_2$. These were 2:1 as composite A, 1:1 as composite B, and 1:2 as composite C. An ultrasound bath (75 kHz, 40% amplitude, pulse 4 s, stop 2 s) with 30 min of pulse total duration was used to disperse the mixture homogeneously. The pH of the ultrasonicated mixture was adjusted with 10 M NaOH until its value reached pH 9. The GO/TiO$_2$ was treated with microwave irradiation heating in a commercial microwave oven Sharp 900 W with 40% power (360 W) for 10 min. Then, the water solvent was evaporated in an ambient condition at 25 °C. Eventually, the dried product was washed with 5% HCl and water three times each until it reached neutral pH. After the washing process, the rGO/TiO$_2$ nanocomposites were dried in an ambient condition at 25 °C. The dried product was recovered as the synthesis result. As a comparison, rGO was synthesized using the aforementioned method without the addition of TiO$_2$.

4.3. Characterization of Structure and Morphology.

The GO and rGO/TiO$_2$ were characterized using various methods. Raman spectroscopy was carried out for GO, its precursor graphite, and rGO/TiO$_2$ by a Raman microscope (Horiba Jobin Yvon, iHR320, Japan) with 1800 I/mm grating, 40 s acquisition, and two accumulations per sample using a 100X objective lens magnification. The excitation light source was a He−Ne laser with a wavelength of 532 nm. The ratios of GO and rGO/TiO$_2$ peaks (D band to G band ratio, I_D/I_G) were calculated from the Raman spectra using the Peak Analyzer from Origin, a scientific data and graphic analysis tool.

Structures and morphologies of rGO/TiO$_2$ were observed using a field-emission scanning electron microscope (FE-SEM) and energy-dispersive X-ray spectroscopy (EDS) with an electron microscope and EDS elemental analysis (Jeol JIB-4610F, Japan) with a Schottky electron gun with a maximum ion current of 200 nA. The samples were gold-coated with a GSL-1100X-SPC-12 Compact Plasma Sputtering Coater. Both low and high magnifications on FE-SEM were used to observe the composites, and EDS mapping for O, Ti, and C elements was conducted. A transmission electron microscope (TEM) instrument (FEI Tecnai G2 20S-Twin, the United States) was also used to observe morphologies at a higher magnification with 200 kV voltage and the distance between sample and electron source of 680 mm.

GO, graphite, TiO$_2$, and rGO/TiO$_2$ nanocomposites were characterized using an X-ray diffraction (XRD) diffractometer (Rigaku SmartLab, Japan) with a Cu Kα light source (λ = 1.54056 Å). For GO and graphite, about 1 g of sample was used with diffraction angle (2θ) between 5 and 60°. On the other hand, about 0.1 g of TiO$_2$ and its nanocomposites was used with diffraction angle (2θ) between 5 and 100°. The interlayer spacing distance (d) of GO and graphite was identified from their highest peak and calculated using Bragg's law with the previously mentioned variables.

GO was characterized even further using ultraviolet−visible (UV−vis) spectroscopy and Fourier transform infrared (FTIR) spectroscopy. The UV−vis spectrum was obtained using a UV−vis spectrometer (Hitachi UH5300, Japan) with wavelength between 190 and 1100 nm. The FTIR spectrum was obtained using an FTIR spectrometer (Thermoscientific Nicolet iS-10) with the wavelength range between 400 and 4000 cm^{-1}. About 5 mg of the GO sample was mixed with potassium bromide (KBr) powder and was manually pressed with the aid of a pressing device.

Further characterizations were conducted on TiO$_2$ and rGO/TiO$_2$ nanocomposites. Diffuse reflectance (DR) UV−vis was conducted with a simple spectrometer with an Ocean Optics DH-mini UV−vis−NIR light source and a high-sensitivity Maya Pro Series (Ocean Optics Inc., FL) as the detector to measure the sample's reflectance.

4.4. Photocatalytic Experiment of Rhodamine 6G.

Photocatalytic performances of TiO$_2$, rGO, and the obtained rGO/TiO$_2$ nanocomposites were determined by studying the dye degradation profile under UV irradiation (λ = 352 nm[64]) for 4 h with rhodamine 6G (R6G) as the dye model. Briefly, six different samples, namely, R6G, rGO, TiO$_2$, composite A, composite B, and composite C, were prepared by mixing 500 mL of R6G solution with 25 mL of catalyst solutions containing DI water, rGO, TiO$_2$, composite A, composite B, and composite C, respectively. The final concentration of R6G and the catalyst in the testing samples was 10 ppm to obtain R6G/catalyst ratio 1:1. All of the samples were mixed until homogeneous right before the experiment began. During photocatalytic experiments, samples were taken at every 15 min time intervals for the first 3 h and at 60 min time intervals at the fourth hour and characterized using UV−vis spectroscopy to determine the R6G concentration in the solution. These concentration values would be divided by the initial R6G concentration to yield the R6G degradation profile (in percentage/%) as a function of UV irradiation time.

Time-resolved photoluminescence (TRPL) was conducted on samples before and after the photocatalysis experiment using TimeHarp 260 from PicoQuant and a picosecond laser at 420 nm wavelength, 20 ps pulse width, 50 mW power, and 10 MHz repetition rate. The laser beam was focused onto the sample, and the emission was then collected into a photon microdevice (PMD) detector. A band-pass filter was placed in front of the detector to get only emission signals at 500 and 550 nm wavelengths. For photoluminescence measurements, the 420 nm laser was focused onto the samples and the emission spectra were recorded using an Aurora4000 spectrometer.

The analysis of time-resolved photoluminescence was done using a two-component exponential decay fitting to get a_i (fractional contribution of decay lifetime, i = 1, 2) and τ_i (decay lifetime, i = 1, 2).

■ AUTHOR INFORMATION

Corresponding Author

Arie Wibowo − Materials Science and Engineering Research Group, Faculty of Mechanical and Aerospace Engineering, Institut Teknologi Bandung, Bandung 40132, Indonesia; Research Center for Nanoscience and Nanotechnology, Institut Teknologi Bandung, Bandung 40132, Indonesia; ⊚ orcid.org/0000-0002-0581-2433; Email: ariewibowo@material.itb.ac.id

Authors

Andri Hardiansyah − Research Center for Physics, Indonesian Institutes of Sciences, Tangerang Selatan, Banten 15314, Indonesia

William J. Budiman − Materials Science and Engineering Research Group, Faculty of Mechanical and Aerospace Engineering, Institut Teknologi Bandung, Bandung 40132, Indonesia

Nurfina Yudasari − *Research Center for Physics, Indonesian Institutes of Sciences, Tangerang Selatan, Banten 15314, Indonesia*

Isnaeni − *Research Center for Physics, Indonesian Institutes of Sciences, Tangerang Selatan, Banten 15314, Indonesia*

Tetsuya Kida − *Division of Materials Science, Faculty of Advanced Science and Technology (Department of Applied Chemistry & Biochemistry), Kumamoto University, Kumamoto 860-8555, Japan;* ⊙ orcid.org/0000-0001-9357-9557

Author Contributions

A.H.: resources, supervision, data analysis, writing—review. W.J.B.: writing the original draft, editing, data acquisition, data analysis. N.Y.: resources, data acquisition. Isnaeni: resources, data acquisition. T.K.: data analysis, writing—review. A.W.: supervision, resources, writing the original draft, writing—review. All authors have given approval to the final version of the manuscript.

Notes

The authors declare no competing financial interest.

■ ACKNOWLEDGMENTS

■ REFERENCES

(1) Nidheesh, P.; Zhou, M.; Oturan, M. A. An overview on the removal of synthetic dyes from water by electrochemical advanced oxidation processes. *Chemosphere* **2018**, *197*, 210−227.

(2) Jamee, R.; Siddique, R. Biodegradation of synthetic dyes of textile effluent by microorganisms: an environmentally and economically sustainable approach. *Eur. J. Microbiol. Immunol.* **2019**, *9*, 114−118.

(3) Wibowo, A.; Marsudi, M. A.; Pramono, E.; Belva, J.; Parmita, A. W. Y. P.; Patah, A.; Eddy, D. R.; Aimon, A. H.; Ramelan, A. Recent Improvement Strategies on Metal-Organic Frameworks as Adsorbent, Catalyst, and Membrane for Wastewater Treatment. *Molecules* **2021**, *26*, No. 5261.

(4) Miklos, D. B.; Remy, C.; Jekel, M.; Linden, K. G.; Drewes, J. E.; Hübner, U. Evaluation of advanced oxidation processes for water and wastewater treatment−A critical review. *Water Res.* **2018**, *139*, 118−131.

(5) Wibowo, A.; Indrawan, R. F.; Triadhi, U.; Aimon, A. H.; Iskandar, F.; Ardy, H. Simple preparation of Fenton catalyst@ bacterial cellulose for waste water treatment. *Mater. Res. Express* **2018**, *5*, No. 024005.

(6) Fang, M.-M.; Shao, J.-X.; Huang, X.-G.; Wang, J.-Y.; Chen, W. Direct Z-scheme CdFe2O4/g-C3N4 hybrid photocatalysts for highly efficient ceftiofur sodium photodegradation. *J. Mater. Sci. Technol.* **2020**, *56*, 133−142.

(7) Gusain, R.; Gupta, K.; Joshi, P.; Khatri, O. P. Adsorptive removal and photocatalytic degradation of organic pollutants using metal oxides and their composites: A comprehensive review. *Adv. Colloid Interface Sci.* **2019**, *272*, No. 102009.

(8) Pirhashemi, M.; Habibi-Yangjeh, A.; Pouran, S. R. Review on the criteria anticipated for the fabrication of highly efficient ZnO-based visible-light-driven photocatalysts. *J. Ind. Eng. Chem.* **2018**, *62*, 1−25.

(9) Mitra, M.; Ahamed, S. T.; Ghosh, A.; Mondal, A.; Kargupta, K.; Ganguly, S.; Banerjee, D. Polyaniline/reduced graphene oxide composite-enhanced visible-light-driven photocatalytic activity for the degradation of organic dyes. *ACS Omega* **2019**, *4*, 1623−1635.

(10) Li, X.; Xie, J.; Jiang, C.; Yu, J.; Zhang, P. Review on design and evaluation of environmental photocatalysts. *Front Environ. Sci. Eng.* **2018**, *12*, No. 14.

(11) Wang, J.; Wang, G.; Cheng, B.; Yu, J.; Fan, J. Sulfur-doped g-C3N4/TiO2 S-scheme heterojunction photocatalyst for Congo Red photodegradation. *Chin. J. Catal.* **2021**, *42*, 56−68.

(12) Wang, Y.; Shen, S. Progress and prospects of non-metal doped graphitic carbon nitride for improved photocatalytic performances *Acta Phys. Chim. Sin.* **2020**, 3631905080.

(13) Li, X.; Liu, J.; Huang, J.; He, C.; Feng, Z.; Chen, Z.; Wan, L.; Deng, F. All organic S-scheme heterojunction PDI-Ala/S-C3N4 photocatalyst with enhanced photocatalytic performance. *Acta Phys. Chim. Sin.* **2021**, *37*, No. 2010030.

(14) Sobhani, A.; Salavati-Niasari, M. Transition metal selenides and diselenides: Hydrothermal fabrication, investigation of morphology, particle size and and their applications in photocatalyst. *Adv. Colloid Interface Sci.* **2021**, *287*, No. 102321.

(15) Monsef, R.; Ghiyasiyan-Arani, M.; Amiri, O.; Salavati-Niasari, M. Sonochemical synthesis, characterization and application of PrVO4 nanostructures as an effective photocatalyst for discoloration of organic dye contaminants in wastewater. *Ultrason. Sonochem.* **2020**, *61*, No. 104822.

(16) Ghanbari, M.; Salavati-Niasari, M. Tl4CdI6 nanostructures: facile sonochemical synthesis and photocatalytic activity for removal of organic dyes. *Inorg. Chem.* **2018**, *57*, 11443−11455.

(17) Zinatloo-Ajabshir, S.; Morassaei, M. S.; Salavati-Niasari, M. Eco-friendly synthesis of Nd2Sn2O7−based nanostructure materials using grape juice as green fuel as photocatalyst for the degradation of erythrosine. *Compos. B. Eng.* **2019**, *167*, 643−653.

(18) Ibhadon, A. O.; Fitzpatrick, P. Heterogeneous photocatalysis: recent advances and applications. *Catalysts* **2013**, *3*, 189−218.

(19) Tang, Q.; An, X.; Lan, H.; Liu, H.; Qu, J. Polyoxometalates/TiO2 photocatalysts with engineered facets for enhanced degradation of bisphenol A through persulfate activation. *Appl. Catal. B* **2020**, *268*, No. 118394.

(20) Hu, J.; Li, H.; Muhammad, S.; Wu, Q.; Zhao, Y.; Jiao, Q. Surfactant-assisted hydrothermal synthesis of TiO2/reduced graphene oxide nanocomposites and their photocatalytic performances. *J. Solid State Chem.* **2017**, *253*, 113−120.

(21) Su, Y.; Chen, P.; Wang, F.; Zhang, Q.; Chen, T.; Wang, Y.; Yao, K.; Lv, W.; Liu, G. Decoration of TiO 2/gC 3 N 4 Z-scheme by carbon dots as a novel photocatalyst with improved visible-light photocatalytic performance for the degradation of enrofloxacin. *RSC Adv.* **2017**, *7*, 34096−34103.

(22) Liu, N.; Chen, X.; Zhang, J.; Schwank, J. W. A review on TiO2-based nanotubes synthesized via hydrothermal method: Formation mechanism, structure modification, and photocatalytic applications. *Catal. Today* **2014**, *225*, 34−51.

(23) Bhanvase, B.; Shende, T.; Sonawane, S. A review on graphene−TiO2 and doped graphene−TiO2 nanocomposite photocatalyst for water and wastewater treatment. *Environ. Technol. Rev.* **2017**, *6*, 1−14.

(24) Subhan, M. A.; Saha, P. C.; Sumon, S. A.; Ahmed, J.; Asiri, A. M.; Rahman, M. M.; AlMamun, M. Enhanced photocatalytic activity and ultrasensitive benzaldehyde sensing performance of a SnO2· ZnO· TiO2 nanomaterial. *RSC Adv.* **2018**, *8*, 33048−33058.

(25) Park, J.; Jin, T.; Liu, C.; Li, G.; Yan, M. Three-dimensional graphene−TiO2 nanocomposite photocatalyst synthesized by covalent attachment. *ACS Omega* **2016**, *1*, 351−356.

(26) Li, D.; Sun, J.; Shen, T.; Song, H.; Liu, J.; Wang, C.; Wang, X.; Zhao, R. Influence of morphology and interfacial interaction of TiO2-Graphene nanocomposites on the visible light photocatalytic performance. *J. Solid State Chem.* **2020**, *286*, No. 121301.

(27) Kumar, K. D.; Kumar, G. P.; Reddy, K. S. Rapid microwave synthesis of reduced graphene oxide-supported TiO2 nanostructures as high performance photocatalyst. *Mater. Today: Proc.* **2015**, *2*, 3736−3742.

(28) Sohail, M.; Xue, H.; Jiao, Q.; Li, H.; Khan, K.; Wang, S.; Zhao, Y. Synthesis of well-dispersed TiO2@ reduced graphene oxide (rGO) nanocomposites and their photocatalytic properties. *Mater. Res. Bull.* **2017**, *90*, 125−130.

(29) Soltani, T.; Lee, B.-K. Low intensity-ultrasonic irradiation for highly efficient, eco-friendly and fast synthesis of graphene oxide. *Ultrason. Sonochem.* **2017**, *38*, 693−703.

(30) Marcano, D. C.; Kosynkin, D. V.; Berlin, J. M.; Sinitskii, A.; Sun, Z.; Slesarev, A.; Alemany, L. B.; Lu, W.; Tour, J. M. Improved Synthesis of Graphene Oxide. *ACS Nano* **2010**, *4*, 4806−4814.

(31) Iskandar, F.; Hikmah, U.; Stavila, E.; Aimon, A. Microwave-assisted reduction method under nitrogen atmosphere for synthesis and electrical conductivity improvement of reduced graphene oxide (rGO). *RSC Adv.* **2017**, *7*, 52391−52397.

(32) Jakhar, R.; Yap, J. E.; Joshi, R. Microwave reduction of graphene oxide. *Carbon* **2020**, *170*, 277−293.

(33) Ain, Q. T.; Haq, S. H.; Alshammari, A.; Al-Mutlaq, M. A.; Anjum, M. N. The systemic effect of PEG-nGO-induced oxidative stress in vivo in a rodent model. *Beilstein J. Nanotechnol.* **2019**, *10*, 901−911.

(34) Jaworski, S.; Wierzbicki, M.; Sawosz, E.; Jung, A.; Gielerak, G.; Biernat, J.; Jaremek, H.; Łojkowski, W.; Woźniak, B.; Wojnarowicz, J.; et al. Graphene oxide-based nanocomposites decorated with silver nanoparticles as an antibacterial agent. *Nanoscale Res. Lett.* **2018**, *13*, No. 116.

(35) Muzyka, R.; Drewniak, S.; Pustelny, T.; Chrubasik, M.; Gryglewicz, G. Characterization of graphite oxide and reduced graphene oxide obtained from different graphite precursors and oxidized by different methods using Raman spectroscopy. *Materials* **2018**, *11*, No. 1050.

(36) Guerrero-Contreras, J.; Caballero-Briones, F. Graphene oxide powders with different oxidation degree, prepared by synthesis variations of the Hummers method. *Mater. Chem. Phys.* **2015**, *153*, 209−220.

(37) Sohail, M.; Saleem, M.; Ullah, S.; Saeed, N.; Afridi, A.; Khan, M.; Arif, M. Modified and improved Hummer's synthesis of graphene oxide for capacitors applications. *Mod. Electron. Mater.* **2017**, *3*, 110−116.

(38) Ţucureanu, V.; Matei, A.; Avram, A. M. FTIR spectroscopy for carbon family study. *Crit. Rev. Anal. Chem.* **2016**, *46*, 502−520.

(39) Rattana; Chaiyakun, S.; Witit-Anun, N.; Nuntawong, N.; Chindaudom, P.; Oaew, S.; Kedkeaw, C.; Limsuwan, P. Preparation and characterization of graphene oxide nanosheets. *Procedia Eng.* **2012**, *32*, 759−764.

(40) Strankowski, M.; Włodarczyk, D.; Piszczyk, Ł.; Strankowska, J. Polyurethane nanocomposites containing reduced graphene oxide, FTIR, Raman, and XRD studies. *J. Spectrosc.* **2016**, *2016*, 1−6.

(41) Stobinski, L.; Lesiak, B.; Malolepszy, A.; Mazurkiewicz, M.; Mierzwa, B.; Zemek, J.; Jiricek, P.; Bieloshapka, I. Graphene oxide and reduced graphene oxide studied by the XRD, TEM and electron spectroscopy methods. *J. Electron Spectrosc. Relat. Phenom.* **2014**, *195*, 145−154.

(42) Yu, L.; Wang, L.; Sun, X.; Ye, D. Enhanced photocatalytic activity of rGO/TiO2 for the decomposition of formaldehyde under visible light irradiation. *J. Environ. Sci.* **2018**, *73*, 138−146.

(43) Liu, X.; Pan, L.; Lv, T.; Zhu, G.; Lu, T.; Sun, Z.; Sun, C. Microwave-assisted synthesis of TiO 2-reduced graphene oxide composites for the photocatalytic reduction of Cr (VI). *RSC Adv.* **2011**, *1*, 1245−1249.

(44) Zhang, Q.; Ma, L.; Shao, M.; Huang, J.; Ding, M.; Deng, X.; Wei, X.; Xu, X. Anodic oxidation synthesis of one-dimensional TiO2 nanostructures for photocatalytic and field emission properties. *J. Nanomater.* **2014**, *2014*, 1−14.

(45) Monshi, A.; Foroughi, M. R.; Monshi, M. R. Modified Scherrer equation to estimate more accurately nano-crystallite size using XRD. *World J. Nano Sci. Eng.* **2012**, *02*, 154−160.

(46) Gonçalves, B. S.; Silva, L. M.; de Souza, T. C.; de Castro, V. G.; Silva, G. G.; Silva, B. C.; Krambrock, K.; Soares, R. B.; Lins, V. F.; Houmard, M.; et al. Solvent effect on the structure and photocatalytic behavior of TiO2-RGO nanocomposites. *J. Mater. Res.* **2019**, *34*, 3918−3930.

(47) AlShammari, A.; Halim, M.; Yam, F.; Kaus, N. Effect of precursor concentration on the performance of UV photodetector using TiO2/reduced graphene oxide (rGO) nanocomposite. *Results Phys.* **2020**, *19*, No. 103630.

(48) Xu, D.; Li, L.; He, R.; Qi, L.; Zhang, L.; Cheng, B. Noble metal-free RGO/TiO2 composite nanofiber with enhanced photocatalytic H2-production performance. *Appl. Surf. Sci.* **2018**, *434*, 620−625.

(49) Zhang, Q.; He, Y.; Chen, X.; Hu, D.; Li, L.; Yin, T.; Ji, L. Structure and photocatalytic properties of TiO 2-graphene oxide intercalated composite. *Chin. Sci. Bull.* **2011**, *56*, 331−339.

(50) Bavykin, D. V.; Parmon, V. N.; Lapkin, A. A.; Walsh, F. C. The effect of hydrothermal conditions on the mesoporous structure of TiO 2 nanotubes. *J. Mater. Chem.* **2004**, *14*, 3370−3377.

(51) Tsai, C.-C.; Teng, H. Structural features of nanotubes synthesized from NaOH treatment on TiO2 with different post-treatments. *Chem. Mater.* **2006**, *18*, 367−373.

(52) Wu, J.; Zhao, J.; Vaidhyanathan, B.; Zhang, H.; Anshuman, A.; Nare, A.; Saremi-Yarahmadi, S. Rapid microwave-assisted bulk production of high-quality reduced graphene oxide for lithium ion batteries. *Materialia* **2020**, *13*, No. 100833.

(53) Minitha, C. R.; Lalitha, M.; Jeyachandran, Y.; Senthilkumar, L.; Rajendra Kumar, R. T. Adsorption behaviour of reduced graphene oxide towards cationic and anionic dyes: Co-action of electrostatic and $\pi-\pi$ interactions. *Mater. Chem. Phys.* **2017**, *194*, 243−252.

(54) Pu, S.; Zhu, R.; Ma, H.; Deng, D.; Pei, X.; Qi, F.; Chu, W. Facile in-situ design strategy to disperse TiO2 nanoparticles on graphene for the enhanced photocatalytic degradation of rhodamine 6G. *Appl. Catal. B* **2017**, *218*, 208−219.

(55) Suave, J.; Amorim, S. M.; Angelo, J.; Andrade, L.; Mendes, A.; Moreira, R. F. TiO2/reduced graphene oxide composites for photocatalytic degradation in aqueous and gaseous medium. *J. Photochem. Photobiol. A* **2017**, *348*, 326−336.

(56) Gayathri, S.; Kottaisamy, M.; Ramakrishnan, V. Facile microwave-assisted synthesis of titanium dioxide decorated graphene nanocomposite for photodegradation of organic dyes. *AIP Adv.* **2015**, *5*, No. 127219.

(57) Nainani, R. K.; Thakur, P. Facile synthesis of TiO2-RGO composite with enhanced performance for the photocatalytic mineralization of organic pollutants. *Water Sci. Technol.* **2016**, *73*, 1927−1936.

(58) Lu, W.-C.; Tseng, L.-C.; Chang, K.-S. Fabrication of TiO2-reduced graphene oxide nanorod composition spreads using combinatorial hydrothermal synthesis and their photocatalytic and photoelectrochemical applications. *ACS Comb. Sci.* **2017**, *19*, 585−593.

(59) Myrick, M. L.; Simcock, M. N.; Baranowski, M.; Brooke, H.; Morgan, S. L.; McCutcheon, J. N. The Kubelka-Munk diffuse reflectance formula revisited. *Appl. Spectrosc. Rev.* **2011**, *46*, 140−165.

(60) Mathew, S.; kumar Prasad, A.; Benoy, T.; Rakesh, P.; Hari, M.; Libish, T.; Radhakrishnan, P.; Nampoori, V.; Vallabhan, C. UV−visible photoluminescence of TiO2 nanoparticles prepared by hydrothermal method. *J. Fluoresc.* **2012**, *22*, 1563−1569.

(61) Tolosana-Moranchel, A.; Casas, J.; Bahamonde, A.; Pascual, L.; Granone, L.; Schneider, J.; Dillert, R.; Bahnemann, D. Nature and photoreactivity of TiO2-rGO nanocomposites in aqueous suspensions under UV-A irradiation. *Appl. Catal. B* **2019**, *241*, 375−384.

(62) Isnaeni; Herbani, Y.; Suliyanti, M. M. Concentration effect on optical properties of carbon dots at room temperature. *J. Lumin.* **2018**, *198*, 215−219.

(63) Sun, M.-Y.; Zheng, Y.-J.; Zhang, L.; Zhao, L.-P.; Zhang, B. Carbon-nanodot-coverage-dependent photocatalytic performance of carbon nanodot/TiO2 nanocomposites under visible light. *Chin. Phys. B* **2017**, *26*, No. 058101.

(64) Yudasari, N.; Anugrahwidya, R.; Tahir, D.; Suliyanti, M. M.; Herbani, Y.; Imawan, C.; Khalil, M.; Djuhana, D. Enhanced photocatalytic degradation of rhodamine 6G (R6G) using ZnO−Ag

nanoparticles synthesized by pulsed laser ablation in liquid (PLAL). *J. Alloys Compd.* **2021**, *886*, No. 161291.

(65) Pant, B.; Park, M.; Park, S.-J. Recent advances in TiO2 films prepared by sol-gel methods for photocatalytic degradation of organic pollutants and antibacterial activities. *Coatings* **2019**, *9*, No. 613.

(66) Hamidah, N. L.; Shintani, M.; Ahmad Fauzi, A. S.; Putri, G. K.; Kitamura, S.; Hatakeyama, K.; Sasaki, M.; Quitain, A. T.; Kida, T. Graphene Oxide Membranes with Cerium-Enhanced Proton Conductivity for Water Vapor Electrolysis. *ACS Appl. Nano Mater.* **2020**, *3*, 4292−4304.